

Subcycle dynamics of electron-hole pairs and high-harmonic generation in bulk diamond subjected to intense femtosecond laser pulse

Tzveta Apostolova, Boyan Obreshkov

Institute for Nuclear Research and Nuclear Energy,

Bulgarian Academy of Sciences, Tsarigradsko chaussee 72, Sofia 1784, Bulgaria

Abstract

We present calculation of photoexcitation and high-harmonic generation in bulk diamond induced by linearly-polarized intense laser pulse of photon energy 1.55 eV, having a time duration of 15 fs and peak field strength $F = 0.4 \text{ V/\AA}$. Depending on the laser polarization direction, the pulsed irradiation creates electron-hole pairs and transient density fluctuations in a localized region of the crystal momentum space, as a consequence energetic intra- and inter-band harmonics are generated with alternating phase during each half-cycle of the driving pulse. The corresponding intra- and inter-band currents are in definite phase relation relative to the driving pulse, reflecting the build-up of coherent superposition of population between valence and conduction bands, and acceleration of charge carriers in their respective bands.

PACS numbers:

I. INTRODUCTION

High-harmonic generation (HHG) is a non-linear process of laser frequency conversion to its multiples driven by the strong coupling of the laser field to electrons. The later-matter interaction results in coherent oscillation of the electrons and its periodicity is illustrated by emission of harmonics. HHG is a way of producing intense attosecond pulses with wavelength extending from the XUV to the soft X-ray region and the steps involved in high harmonic generation are shown to determine the time scale and energy of the generated pulses¹⁻⁴. The application of single-cycle attosecond pulses in the VUV has enabled the tracing of electronic motion and electronic relaxation in atoms and molecules⁵. Femtosecond-laser-driven high harmonic generation sources have been used for coherent diffractive imaging (CDI) of biological samples and magnetic domain patterns with nanoscale resolution^{6,7}. In situ characterization of the transient structural, optical, and electronic properties of single nanoparticles has been achieved recently via CDI using XUV pulses from a HHG source⁸.

The observation of nonperturbative high harmonic generation in a strongly driven bulk of wide-bandgap semiconductor and dielectric materials such as ZnO, GaSe and SiO₂⁹⁻¹² has enabled the exploration of ultrafast electron dynamics in the condensed phase, laying the foundation of attosecond solid-state ultrafast spectroscopy¹³. The interplay between generation of charged carriers via multiphoton or tunnel ionization at high intensities leading to dielectric breakdown, has been carefully explored to find regimes in which only HHG takes place avoiding material damage. Multiple plateaus extending beyond the limit of the corresponding gas phase harmonics⁹ have been observed and linear scaling of the cutoff energy with the laser field has been found. HHG sources from semiconductors and dielectrics have the potential of being brighter owing to the high atomic density of the target material and the ability to withstand the driving laser fields necessary for inducing strong nonlinear and non perturbative effects underlying the production of high harmonic radiation. Furthermore ultrafast nonlinear transient reversible electric currents below damage threshold can be experimentally generated in dielectrics¹⁴, with potential applications in modern electronics and petahertz-scale signal processing^{16,17}. Numerical simulations based on time-dependent density functional theory gave insight into atomic-scale properties of the induced ultrafast currents¹⁵; these results suggest that an intense laser fields distort the electronic band structure and transform an insulator transiently into a metal on a sub-femtosecond time scale.

Theoretical models have been proposed to analyze HHG in crystalline solids, using first principle approaches,^{19–23} time-dependent-Schrodinger-equation (TDSE)^{24,25}, semiconductor Bloch equations^{10,26} and semiclassical re-collision models²⁷. The theory has identified two main mechanisms of HHG in solids, based on distinction between physical effects associated with intra- and interband motion of photoexcited carriers, though in actual computation of HHG spectra these contributions are entangled. In Ref.²⁷, the relative importance of these two mechanisms was investigated over a wide range of wavelengths. For mid-IR lasers, generation of harmonic photons is dominated by interband mechanism, in contrast, for far-infrared incident laser frequencies, intraband emission arising from nonlinear band velocities (i.e. non-parabolic energy-momentum dispersion law) becomes dominant. Similarly to HHG in the gas phase^{28,29}, the interband emission in solids can be modelled semi-classically in terms of trajectories of electron-hole pairs in the laser electric field; it gives a simple approximate law for the harmonic cutoff energy in solids; usually the maximum cutoff energy for HHG is limited by the maximum band gap that can be reached by an electron-hole pair during one optical cycle of the laser field. In Ref.^{30,31}, HHG in model one-dimensional crystals were studied numerically, for instance Ref.³⁰ proposed a simplified momentum space analogue of the semi-classical three-step model for HHG in the gas phase, including tunnel ionization into a conduction band, acceleration of electrons and valence band holes in their respective bands, followed by their radiative recombination with emission of a single short wavelength photon. Importantly, such type of models incorporate the multi-band structure of the solid, and successfully reproduce the experimentally observed multi-plateau structure of HHG in rare-gas solids (cf. also Ref.²⁵). However reduced dimensionality models do not incorporate realistic three-dimensional static band-structures, also the crystal-momentum-dependence of couplings between valence and conduction bands is rarely discussed in the context of HHG.

In the present work we focus on specific aspects of HHG associated with subcycle dynamics of photoexcited electron-hole pairs in diamond bulk driven by linearly polarized intense 15 fs laser pulse with 800nm wavelength. The paper is organized as follows: Section II presents the theoretical scheme for modelling photo-excitation and photoionization of diamond bulk. Section III is divided into three sub-sections: the first one includes description of the static band structure of diamond and the crystal-momentum dependence of the transition dipole matrix element; the second one presents some analytic results and analysis of HHG within

a simplified two-band model, the third subsection includes numerical results of a full multi-band model that unveal the relative importance of interband and intraband dynamics of photoexcited carriers in diamond. Sec. IV includes our main conclusions. Atomic units are used $e = \hbar = m_e = 1$ throughout this paper.

II. PSEUDOPOTENTIAL METHOD

We describe the electron dynamics in a unit cell of crystalline diamond subjected to spatially uniform laser electric field $\mathbf{F}(t)$ with the time-dependent Schrödinger equation in single-active electron approximation

$$i\partial_t|\psi_{v\mathbf{k}}(t)\rangle = H(t)|\psi_{v\mathbf{k}}(t)\rangle, \quad (1)$$

where $v\mathbf{k}$ labels the initially occupied valence band states of definite crystal momentum \mathbf{k} and

$$H(t) = \frac{1}{2}[\mathbf{p} + \mathbf{A}(t)]^2 + V(\mathbf{r}), \quad (2)$$

is the time-dependent Hamiltonian in velocity gauge with $\mathbf{F}(t) = -\partial_t\mathbf{A}(t)$, here $\mathbf{A}(t)$ is the laser vector potential, $\mathbf{p} = -i\nabla_{\mathbf{r}}$ is the momentum operator and $V(\mathbf{r})$ is the periodic ion-lattice potential. In the local empirical pseudopotential method³², the scalar potential is presented in a plane wave expansion in the basis of reciprocal lattice wave-vectors \mathbf{G}

$$V(\mathbf{r}) = \sum_{\mathbf{G}} V(G) \cos(\mathbf{G} \cdot \boldsymbol{\tau}) e^{i\mathbf{G} \cdot \mathbf{r}}, \quad (3)$$

here $2\boldsymbol{\tau} = a_0(1/4, 1/4, 1/4)$ is a relative vector connecting two carbon atoms in a crystal unit cell and $a_0 = 3.57 \text{ \AA}$ is the bulk lattice constant. In Eq.(3), the pseudopotential formfactors $V(G)$ (in Rydberg) are $V(G^2 = 3) = -0.625$, $V(G^2 = 8) = 0.051$, and $V(G^2 = 11) = 0.206$; here the wave number G is measured in units of $2\pi/a_0$.

To solve Eq.(1) we use a basis set expansion over static Bloch states $|n\mathbf{k}\rangle$ with associated eigenenergies $\varepsilon_{n\mathbf{k}}$, which are solutions of the field-free Schrödinger equation $[\mathbf{p}^2/2 + V]|n\mathbf{k}\rangle = \varepsilon_{n\mathbf{k}}|n\mathbf{k}\rangle$, i.e. we write the expansion

$$|\psi_{v\mathbf{k}}(t)\rangle = \sum_n a_{nv}(\mathbf{k}, t) |n\mathbf{k}\rangle. \quad (4)$$

Substiuting Eq.(4) into Eq.(1) gives a set of coupled equations for the transition amplitudes

$$i\partial_t a_{nv}(\mathbf{k}, t) = \varepsilon_{n\mathbf{k}} a_{nv}(\mathbf{k}, t) + \sum_{n'} \mathbf{A}(t) \cdot \mathbf{p}_{nn'}(\mathbf{k}) a_{n'v}(\mathbf{k}, t), \quad (5)$$

which are subject to initial conditions specified in the remote past $a_{nv}(\mathbf{k}, t \rightarrow -\infty) = \delta_{nv}$. The matrix representation of the momentum operator is

$$\mathbf{p}_{nn'}(\mathbf{k}) = \mathbf{k}\delta_{nn'} + \sum_{\mathbf{G}} \mathbf{G}c_{n,\mathbf{G}+\mathbf{k}}^*c_{n',\mathbf{G}+\mathbf{k}} \quad (6)$$

where $c_{n,\mathbf{G}+\mathbf{k}}$ are the Fourier coefficients in the expansion of the Bloch orbitals over plane waves. The laser vector potential was assumed to be a temporally Gaussian pulse $\mathbf{A}(t) = \mathbf{e} \exp(-\ln(4)t^2/\tau^2) \sin \omega_L t$, where $\hbar\omega_L=1.55$ eV is the photon energy, $\tau = 15$ fs is the pulse duration and \mathbf{e} is a unit vector in the direction of polarization. The relevant output of the calculation are the time-dependent occupation numbers of Bloch states

$$f_{n\mathbf{k}}(t) = \sum_v |\langle n\mathbf{k}|\psi_{v\mathbf{k}}(t)\rangle|^2, \quad (7)$$

the transient distribution function of conduction electrons

$$f_e(\mathbf{k}, t) = \sum_c f_{c\mathbf{k}}(t), \quad (8)$$

and the total number of electrons at time t

$$n_e(t) = \int_{\text{BZ}} \frac{d^3\mathbf{k}}{4\pi^3} f_e(\mathbf{k}, t). \quad (9)$$

The instantaneous absorbed energy in a unit cell of the diamond lattice is

$$\Delta E(t) = \sum_v \int_{\text{BZ}} \frac{d^3\mathbf{k}}{4\pi^3} \langle \psi_{v\mathbf{k}}(t)|i\partial_t|\psi_{v\mathbf{k}}(t)\rangle - E_0, \quad (10)$$

where E_0 is the ground state energy. After the end of the pulse ($t \rightarrow \infty$), the absorbed energy can be expressed by change of the occupation of single-particle states

$$\Delta E(\infty) = \sum_n \int_{\text{BZ}} \frac{d^3\mathbf{k}}{4\pi^3} \varepsilon_{n\mathbf{k}} [f_{n\mathbf{k}}(\infty) - f_{n\mathbf{k}}^0] \quad (11)$$

where $f_{v\mathbf{k}}^0 = 1$ and $f_{c\mathbf{k}}^0 = 0$. In the electron-hole picture with $f_{c\mathbf{k}} = f_{e\mathbf{k}}$, $f_{v\mathbf{k}} = 1 - f_{h-\mathbf{k}}$, $\varepsilon_{h\mathbf{k}} = -\varepsilon_{v\mathbf{k}}$ and $\varepsilon_{c\mathbf{k}} = \varepsilon_{e\mathbf{k}}$, the absorbed energy $\Delta E(\infty) = \sum_{h,\mathbf{k}} f_{h\mathbf{k}}\varepsilon_{h\mathbf{k}} + \sum_{e,\mathbf{k}} f_{e\mathbf{k}}\varepsilon_{e\mathbf{k}}$ is exclusively due to production of electron-hole pairs.

The optically-induced electron current density is given by the BZ integral

$$\mathbf{J}(t) = \int_{\text{BZ}} \frac{d^3\mathbf{k}}{4\pi^3} \mathbf{J}(\mathbf{k}, t) \quad (12)$$

where

$$\mathbf{J}(\mathbf{k}, t) = \sum_v \langle \psi_{v\mathbf{k}}(t) | \mathbf{v}(t) | \psi_{v\mathbf{k}}(t) \rangle, \quad (13)$$

and $\mathbf{v}(t) = \mathbf{p} + \mathbf{A}(t)$ is the velocity operator. From the time-dependent current density, the spectrum of high order harmonics can be calculated as a coherent sum

$$I(\omega) = \left| \int_{\text{BZ}} \frac{d^3\mathbf{k}}{4\pi^3} J_{\mathbf{k},\omega} \right| \quad (14)$$

over contributions from Bloch states with quasi-momentum \mathbf{k}

$$J_{\mathbf{k},\omega} = \int dt e^{i\omega t} \mathbf{e} \cdot \mathbf{J}(\mathbf{k}, t). \quad (15)$$

III. NUMERICAL RESULTS AND DISCUSSION

A. Static band structure and matrix elements

The static energy-band structure of diamond along the Δ and Λ lines is shown in Fig.1. The pseudopotential model reproduces quantitatively the principal energy gaps and the optical properties of diamond in the UV region³³. The location of the conduction band minimum at $\mathbf{k} = (0.8, 0, 0)$ relative to the valence band maximum at Γ , specifies the threshold for indirect transitions 5.42 eV. The prominent direct bandgap transitions are $\Gamma_{25'} \rightarrow \Gamma_{2'}$ (7.1 eV), $\Gamma_{25'} \rightarrow \Gamma_{15}$ (10 eV), $L_{3'} \rightarrow L_{2'}$ (8 eV), $L_{3'} \rightarrow L_3$ (13.1 eV), $X_4 \rightarrow X_1$ (11.5 eV). Thus the threshold for direct transitions is assigned to the $\Gamma_{25'} \rightarrow \Gamma_{2'}$ transition and the main UV absorption peak can be assigned to the $X_1 \rightarrow X_4$ interband transition. An important difference with regard to other band structure calculations is the energy level ordering at Γ and L: the pseudopotential parameters used in our calculation predict $\Gamma_{2'}$ lower in energy than Γ_{15} , as a consequence $L_{2'}$ is also lower in energy than the L_1 and L_3 conduction bands (cf. also Ref.³⁴).

In Fig.2 we show the squared matrix elements $|\langle \Lambda_{1,th} | \mathbf{e} \cdot \mathbf{p} | \Lambda_{1,c} \rangle|^2$ and $|\langle \Lambda_{1,th} | \mathbf{e} \cdot \mathbf{p} | \Lambda_{3,c} \rangle|^2$ between the light hole and the lowest two conduction bands, for laser linearly polarized along the [111] direction (cf. also Fig. 1); for this specific laser polarization, the couplings among the heavy hole and these conduction bands vanish $\langle \Lambda_{3,hh} | \mathbf{e} \cdot \mathbf{p} | \Lambda_{1,c} \rangle = \langle \Lambda_{3,hh} | \mathbf{e} \cdot \mathbf{p} | \Lambda_{3,c} \rangle = 0$. Noticeably the interactions with the light hole exhibit sensitive momentum dependence and are well localized near the BZ center, i.e. the $\Gamma_{25'} \rightarrow \Gamma_{2'}$ and $\Gamma_{25'} \rightarrow \Gamma_{15'}$

interband transitions should give dominant contribution for the photoexcitation and HHG. It is worth to note that some authors assume constant value for the interband momentum matrix element³⁵, which may be good approximation for semiconductors³⁶, however we find that the detailed momentum-dependence of the interband couplings should be accounted for HHG in widebandgap solids such as diamond.

B. Time-dependent interactions

1. Two band model

To examine the relevance of interband couplings and field-induced distortion of the diamond band structure, we develop a simplified two band model describing the interactions between the light hole and the lowest conduction band $M_k = \langle \Lambda_{1,c} | \mathbf{e} \cdot \mathbf{p} | \Lambda_{1,th} \rangle$ for laser irradiation linearly polarized along the [111] direction. For this specific direction in the BZ, $\mathbf{k} = k(1, 1, 1)$, the equations of motion Eq.(5) simplify to

$$\begin{aligned} i\partial_t a_k^{(\Lambda_{1,th})}(t) &= \varepsilon_k^{(\Lambda_{1,th})}(t) a_k^{(\Lambda_{1,th})}(t) + A(t) M_k a_k^{(\Lambda_{1,c})}(t) \\ i\partial_t a_k^{(\Lambda_{1,c})}(t) &= \varepsilon_k^{(\Lambda_{1,c})}(t) a_k^{(\Lambda_{1,c})}(t) + A(t) M_k a_k^{(\Lambda_{1,th})}(t) \end{aligned}$$

here $\varepsilon_k^{(\Lambda_{1,th})}(t) = \varepsilon_k^{(\Lambda_{1,th})} + A(t) v_k^{(\Lambda_{1,th})}$ is a time-dependent energetic shift of the light hole band, $v_k^{(\Lambda_{1,th})} = \mathbf{e} \cdot \nabla_{\mathbf{k}} \varepsilon_k^{(\Lambda_{1,th})}$ is the velocity of the light hole projected onto the laser polarization direction, similarly the conduction band undergoes an ultrafast level shift $\varepsilon_k^{(\Lambda_{1,c})}(t) = \varepsilon_k^{(\Lambda_{1,c})} + A(t) v_k^{(\Lambda_{1,c})}$. We further assume that the occupation of the light hole band can be neglected (i.e. we neglect the depletion of the ground state), and the main effect of the oscillating electric field is to induce temporal fluctuation of the valence band energy, i.e.

$$a_k^{(\Lambda_{1,th})}(t) \approx \exp \left(-i \int_{-\infty}^t dt' \varepsilon_k^{(\Lambda_{1,th})}(t') \right). \quad (16)$$

Using this approximation, the photoionization amplitude becomes

$$a_k^{(\Lambda_{1,c})}(t) \approx -i M_k e^{-i S_k(t)} \int_{-\infty}^t dt' e^{i \Delta_k t'} e^{i \xi(t') v_k} A(t') \quad (17)$$

where $S_k(t) = \int_{-\infty}^t dt' \varepsilon_k^{(\Lambda_{1,c})}(t')$ is the quasiclassical action for conduction electron, $\Delta_k = \varepsilon_k^{(\Lambda_{1,c})} - \varepsilon_k^{(\Lambda_{1,th})}$ is the bandgap energy, $v_k = v_k^{(\Lambda_{1,c})} - v_k^{(\Lambda_{1,th})}$ is the relative speed between an

electron and the light hole and $\xi(t) = \int_0^t dt' A(t')$. For monochromatic laser $\xi(t) = \xi \cos \omega_L t$, where $\xi = F/\omega_L^2$ is the excursion length in the oscillatory motion of a free electron, we use the expansion in Fourier-Bessel series

$$e^{ix \cos \theta} = \sum_{l=-\infty}^{\infty} i^l e^{il\theta} J_l(x), \quad (18)$$

with the definition of a phase angle $\theta = \omega_L t$, the photoionization amplitude can be written as

$$a_k^{(\Lambda_{1,c})}(t) = e^{-iS_k(\theta)} \frac{FM_k}{2\omega_L} \sum_l i^l J_l(\xi v_k) e^{il\theta} \left(\frac{e^{i\theta}}{\Delta_k + (l+1)\omega_L + i\eta} - \frac{e^{-i\theta}}{\Delta_k + (l-1)\omega_L + i\eta} \right) \quad (19)$$

where $\eta = 1/\tau_L > 0$ is a positive infinitesimal. The corresponding distribution function of conduction electrons is a phase-sensitive quantity

$$f_k(\theta) = |a_k^{(\Lambda_{1,c})}(t)|^2 = \sum_l i^l e^{il\theta} f_{kl}, \quad (20)$$

with

$$f_{kl} = M_k^2 \frac{\omega_L^2}{v_k^2} \sum_m m(m-l) \frac{J_m(\xi v_k) J_{m-l}(\xi v_k)}{[\Delta_k + m\omega_L + i\eta][\Delta_k + (m-l)\omega_L - i\eta]}. \quad (21)$$

For each fixed harmonic order l , the Fourier coefficients in Eq.(21) describe interference between elementary multiphoton transitions (both energy-conserving and virtual), the terms with $m < 0$ correspond to multiple absorption of laser photons, while terms with $m > 0$ to stimulated emission of photons. The coefficients satisfy the relation $f_{kl} = (-1)^l f_{-kl}$, which implies that only even order harmonics contribute to the conduction electron density $n(\theta) = \sum_k f_k(\theta)$, in contrast the Fourier expansion of the current includes only odd order harmonics (e.g. the intraband current $J(\theta) = \sum_k f_k(\theta) v_k^{(\Lambda_{1,c})} + J_D(\theta)$, where $J_D = A(\theta) \sum_k f_{k0}$ is a gauge current due to plasma oscillations of the electron gas as a whole), because the band velocities reverse sign $\mathbf{v}_n(-\mathbf{k}) = -\mathbf{v}_n(\mathbf{k})$ under the inversion $\mathbf{k} \rightarrow -\mathbf{k}$.

The density distribution function in Eq.(20) can be split $f_k(\theta) = f_{k0} + \delta f_k(\theta)$ into cycle-averaged distribution f_{k0} and temporal fluctuations $\delta f_k(\theta)$ that describe the emergence of sub-cycle structure in the conduction electron density. In Fig.2a-c we plot the cycle-averaged occupations $f(k) = f_{k0}$, the strength of the density fluctuations $|f_{kl}|$ with $l = 1, 3, 5, \dots$ and the momentum-dependent phase shifts $\delta_{kl} = \text{Arg}[f_{kl}]$, respectively, for the specific excursion

length $\xi = 2.4$. The cycle-averaged distribution in Fig.2a is structured by four sharp peaks near the Γ point: two inner peaks near $|k_5| = 0.025$ and two outer peaks at $|k_6| = 0.06$, the length of k_m is fixed by energy conservation $\Delta_k = -m\omega_L$ (with $m < 0$). Noticeably each of these four conduction states is occupied by nearly half an electron, i.e. neglecting depletion of the ground state is not well justified, thus a more rigorous treatment should carefully account for population inversion of a state \mathbf{k} in terms of the Pauli blocking factor $f_{v\mathbf{k}} - f_{c\mathbf{k}}$.

The density-dependent parameters $\{|f_{kl}|, l = 1, 3, 5, \dots\}$ that are associated with sub-cycle dynamics of electron-hole pairs and HHG are shown in Fig. 2b. The intensity of these odd-order harmonics is weaker than the cycle-averaged yield, the strength of the fundamental harmonic ($l = 1$) displays a broad shoulder interpolating between the threshold wave-numbers k_5 and k_6 , which makes evident the contribution of energetically closed multiphoton channels associated with creation of virtual electron-hole pairs. That is because near k_5 , the argument of the Bessel function $|\xi v_{k_5}| = 1.65 > 1$ enhances the contributions of closed multiphoton channels with $-3 \leq m \leq 3$ in Eq.(21). Near $k = k_6$, the relative speed v_k attains maximum and the argument of the Bessel function increases to $|\xi v_{k_6}| = 2.75$, however the coupling M_{k_6} between the valence and the conduction band is reduced near that point (cf. Fig.2), which in turn weakens the intensity of density fluctuations with k_6 . When the harmonic order is increased to $l = 3$, the distribution becomes more localized in momentum space and moves towards the threshold wave-numbers k_5 and k_6 . Noticeably when the harmonic order is increased to $l = 5$, the strength of that harmonic is diminished near the 5-photon threshold due to destructive interference between $m = 1$ with $m = 2, 3$ closed multiphoton channels. However near the 6-photon threshold k_6 , the energetically open $m = -1$ channel (involving energy-conserving 6-photon transition, followed by absorption of one additional laser photon) interferes with energetically closed channels involving $m = 1, 2, 3$, which in turn enhances the strength of 5-th harmonic near the 6-photon threshold. Quite similarly, the 7th harmonic is enhanced near the 5-photon threshold, that is because $m = 2$ channel is open near k_5 and interferes constructively with nearby closed channels; the 5th and 7th harmonics are almost of equal strength near the 6-photon threshold. The intensity of these harmonics falls off rapidly when $l > 9$, thus $l = 9$ also specifies a cutoff energy for HHG (for these specific parameters of the laser field); by increasing the excursion length ξ the cutoff energy for HHG also increases.

The interference effects involving exchanges of multiple laser photons give rise to sensitive

momentum-dependence of the phase shifts δ_{kl} as shown in Fig.2c; for $l = 1$ the phase shift is appreciably less than $\pi/2$ along the entire Λ -line, such that the fundamental harmonic lags behind the laser electric field by $\pi/2$, and thus follows the temporal profile of the laser vector potential. The phase shift δ_{k3} associated with the generation of the 3rd harmonic exhibits more sensitive momentum dependence and rises above $\pi/2$ near both the 5- and 6-photon thresholds. It is tempting to associate the energy derivative of the phase shift $d\delta/d\varepsilon = (d\delta/dk)/v_k$ with a Wigner-Smith-type time delay, however definition of ionization time delays is subtle in a multiphoton regime. For $l = 5$, δ_{k5} jumps by a little less than π above the 5-photon threshold, which produces a small kink in the amplitude factor $|f_{k5}|$, subsequently the phase function decreases more or less suddenly by π near the 6-photon threshold, which is due to the formation of 6-photon resonance of Breit-Wigner type. Phase shifts associated with the 7th and 9th harmonics are almost indistinguishable as a function of k , the phase jumps by π near the 5- and 6-photon thresholds clearly demonstrate the emergence of isolated Breit-Wigner type resonance profiles in the multiphoton ionization of bulk diamond.

Fig.3 shows the distribution function $f_k(\theta)$, photoelectrons are born at the extrema of the electric field and occupy localized quasimomentum states near k_5 and k_6 due to energy-conserving 5- and 6-photon transitions, respectively. When the electric field reverses direction the distribution broadens and a subcycle structure emerges. During the first quarter of the cycle, the occupation of the conduction band is greatly enhanced in the region of negative wave-numbers $-0.06 < k < -0.025$. This enhancement of the phase-sensitive density is due to hybridization and beating of $l = 1$ with $l = 2$ harmonics; using the expansion $\delta f_k(\theta) = 2 \sum_{l>0} |f_{kl}| \cos(l\theta + \delta_{kl} + l\pi/2)$ and the phase relation $\delta_{kl} = \delta_{-kl} + l\pi$, we find that in the region of positive $k > 0$ near $\theta = \pi/2$ (zero of the electric field) the some density fluctuations interfere destructively with $|f_{k2}| \cos \delta_{k2} - |f_{k1}| \cos \delta_{k1} \approx 0$, which is because the amplitudes $|f_{k1}| \approx |f_{k2}|$ are of the same magnitude and the phase lag $\delta_{k,2} - \delta_{k,1} \ll \pi$ is appreciably small. In contrast the relative phase $\delta_{k2} - \delta_{k1} \approx \pi$ in the range $-0.06 < k < -0.025$, so that the two harmonics add up constructively giving rise to transient enhancement in the number of conduction electrons in that range. At the same time, the destructive interference of these two harmonics enhances the contribution of energetic density fluctuations with $l \geq 3$ near $k_5 = 0.025$ and $k_6 = 0.06$. The various harmonic orders interfere destructively at the half-cycle with $\theta = \pi$. During the next two quarters of the

optical cycle, the distribution repeats itself but with alternating phase, e.g. for $\theta = 3\pi/2$ the electron occupation is enhanced in the positive wave-number range $0.025 < k < 0.06$ due to constructive interference between $l = 1$ and $l = 2$ harmonics, the generation of rapid density fluctuations becomes localized near the negative threshold wave-numbers $k_5 = -0.025$ and $k_6 = -0.06$. However, the conduction electron density is insensitive to the phase relations between odd and even harmonics, because odd order harmonics interfere destructively $n(\theta) = \sum_{k>0, l \geq 0} \varepsilon_l |f_{kl}| \cos(l\theta + \delta_{kl} + l\pi/2)[1 + (-1)^l]$ (here $\varepsilon_l = 1$ for $l = 0$ and $\varepsilon_l = 2$ for $l = 1, 2, \dots$). So that to good approximation the transient fluctuation in the number of conduction electrons can be approximated with $\delta n(\theta) \approx -2 \sum_k |f_{k2}| \cos 2\theta$.

2. Multiband model

In the multiband model based on Eqs.(5), the Brillouin zone (BZ) was sampled by a Monte Carlo method using 3000 randomly generated \mathbf{k} -points, $N = 20$ bands were included in the expansion of the wave-packet over Bloch orbitals, including 4 valence and 16 conduction bands. The wave-functions of initially occupied valence band states were propagated forward in time by applying the Cayley transformation for small equidistant time steps of $\delta t = 0.03$ a.u.

In Fig. 5(a-b), we plot the time evolution of the electron density and the excitation energy per unit cell for peak laser field strength $F = 0.4 \text{ V/\AA}$. The total number of electron-hole pairs increases gradually on the rising edge of the pulse. Charge carriers are born at the extrema of the electric field, their number density increases rapidly during the first quarter of each cycle and attains maximum at the time when the electric field reverses direction, subsequently electrons recombine with their corresponding valence band holes during each second quarter of the cycle, resulting in transient charge density oscillations, in good qualitative agreement with the prediction of the two-band model. After the peak intensity, some large fraction of carriers recombine, such that the cycle-averaged electron yield gradually decreases and stabilizes in the wake of the pulse. The electronic excitation energy is shown in Fig.5(b): the temporal fluctuations of the absorbed energy are tiny and almost negligible, the cycle-averaged energy deposited onto electrons reaches 0.1 eV per unit cell at the pulse peak, well below the cohesive energy of diamond (about 7 eV). Recombination of electron-hole pairs after the pulse peak reduces substantially the energy

gain to 10^{-3} eV/unit cell after conclusion of the pulse.

In Fig.6(a-b), we plot the density of conduction states and the electron distribution function after the end of the pulse. Photoelectrons are excited across the direct bandgap at the Γ point and occupy the $\Gamma_{2'}$ band with energies 2 eV above the conduction band minimum. Noticeably however substantial fraction of carriers are promoted into the Γ_{15} band with energies 5 eV above the conduction band minimum (cf. Fig.6(a)). The asymptotic momentum distribution shown in Fig.6(b) is almost symmetric under spatial inversion with $\mathbf{k} \rightarrow -\mathbf{k}$, electrons occupy states with quasimomentum in a narrow range near the BZ center. Two groups of occupied conduction states can be distinguished: states in the Γ_{15} band produce the inner peaks of the distribution, while the states in the outer two peaks with $k = \pm 0.05$ are due to excitation into the Γ_{15} band. While occupation of the $\Gamma_{2'}$ band is due to interband transition $\Gamma_{25'} \rightarrow \Gamma_{2'}$, the population of the Γ_{15} band is primary due to indirect interaction with $\Gamma_{2'}$ band. That is because the electric field breaks the symmetry of the diamond lattice under spatial inversion, as result the two conduction bands are mixed with the valence band $\Gamma_{25'}$, which enables transfer of population from the $\Gamma_{2'}$ to Γ_{15} band during the irradiation. The comparison of this result with the prediction of our simplified two band model including only the coupling between the light hole and the lowest conduction band, makes evident that the effect of interaction between multiple conduction bands can not be neglected for the photoionization of diamond bulk.

The time evolution of the phase-sensitive electron distribution function $f_e(\mathbf{k}, t)$ is shown in Fig. 7(a-b). The laser excites photoelectrons close to the BZ center because of the localized character of the interactions between the light hole and conduction bands (cf. Fig.(2)). During each two adjacent half-cycles of the driving field, the distribution exhibits the symmetry trend

$$f_e(\mathbf{k}, t) \approx f_e\left(-\mathbf{k}, t \pm \frac{\pi}{\omega_L}\right), \quad (22)$$

which is because for monochromatic laser irradiation $F(t) = F \cos \omega_L t$, the Hamiltonian remains invariant under the combined transformation of spatial inversion $\mathbf{r} \rightarrow -\mathbf{r}$ supplemented by the time translation on half of the laser period $t \rightarrow t \pm \pi/\omega_L$. For pulsed laser irradiation this discrete symmetry is broken by the finite pulse duration τ , however remnants of that symmetry remain prominent, so that electrons move rapidly back and forth about the BZ center during each half-cycle of the laser field. Electron-hole pairs are born at the extrema of the laser electric field, their occupation number increases dramatically

during the first quarter of each cycle, these virtual pairs pop-out of existence during the second quarter of the cycle, at the time when the field reverses direction. During the third quarter of the cycle, electrons re-emerge in the conduction band following the trend of Eq. 22. In very good agreement with the prediction of our two-band model, sub-cycle structure and fine details in the transient density distribution are exhibited when the intensity of the laser increases, the asymptotic distribution ($t \rightarrow \infty$) of real electron-hole pairs is structured into four narrow peaks symmetrically displaced about the BZ center.

The time-development of the HHG current is also shown in Fig.8(a), together with the corresponding HHG spectrum in Fig.8(b). The laser induces reversible ultrafast currents following the temporal profile of the laser vector potential. The HHG spectrum is characterized by odd harmonics structure with plateau region and sharp cutoff at the position of the 9th harmonic. In fact, the position of the cutoff is in good quantitative agreement with the prediction of the two band model, because the strength of the transient density fluctuations is substantially reduced when $l > 9$. The suppression of even order harmonics is a consequence of the approximate symmetry relation $J(\mathbf{k}, t) \approx -J(-\mathbf{k}, t \pm \pi/\omega_L)$, which implies that all even order harmonics interfere destructively.

The total current can be conventionally split into intra- and interband currents, since HHG is a non-linear process, the spectrum of high-order harmonics is not affected by the transformation $J(t) \rightarrow J(t) + J_D(t)$, where $J_D(t) = const \times A(t)$ is the Drude current due to collective plasma oscillation of the electron gas. This splitting allows us to expose the relevant non-linear effects associated with intra- and interband motion of charge carriers. In Fig.9(a) we show the intraband current along the Λ line, by excluding the Drude current and Fig.9(b) shows the interband current shifted by the Drude current. The currents follow the periodicity of the laser vector potential. The intraband current vanishes and exhibits stationary inflection points at the extrema of the electric field due to destructive interference of laser-induced density fluctuations (cf. Sec. IIIa); near the extrema of the electric field, charge carriers decelerate in their respective bands and reverse their speeds, during this transient phase their kinetic energy can be converted into a photon, quite similarly to the bremsstrahlung process. High-order harmonics are emitted in the diamond bulk during each half-cycle with alternating phase (i.e. only odd order harmonics are emitted). Similarly the interband current follows the period of the laser vector potential, but flows in direction opposite to the intraband current. The rapid sub-cycle structure exhibited in the interband

current is a direct consequence of the build-up of coherent superposition of populations in the valence and conduction bands. During each half-cycle, the rapidly oscillating dipole emits radiation in the form of high-order harmonics. Fig.9(c) shows that for the specific 800 nm wavelength, interband harmonics are much more intense in the plateau and cutoff regions, while the intraband current has prominent contribution in the generation of sub-bandgap harmonics.

IV. CONCLUSION

In summary, we have investigated the sub-cycle dynamics of electron-hole pairs and the high harmonic generation in bulk diamond subjected to intense ultrashort laser pulse. For the specific laser wavelength 800 nm, pulse duration 15fs and peak field strength 0.4 V/\AA , we compared the relative importance of two main mechanisms of HHG: intraband emission at each half-cycle of the laser field, which arises due to build-up of rapid sub-cycle fluctuations in the density distribution of photoexcited carriers in momentum space and the interband emission arising due to build-up of non-linear polarization. We also find that the HHG spectrum of the interband current dominates the plateau region of HHG, while the intraband current has primary contribution in the sub-bandgap region. The laser field induces intense interband transitions $\Gamma_{25'} \rightarrow \Gamma_{2'}$, consequently a non-linear intraband current due to transiently asymmetric occupation of the $\Gamma_{2'}$ band is produced (and a hole current due to depletion of the $\Gamma_{25'}$ band). This distortion of the substrate band structure occurs on a sub-femtosecond time scale, transforming diamond into a transiently metallic state supporting non-linear ultrafast currents that are in definite phase relation relative to driving laser field and generate high order harmonics during each half cycle of the pulse.

Acknowledgements

This work is supported by the Bulgarian National Science Fund under Contract No. DFNI-E02/6 and Contract No. DNTS/France-01/9 (T.A.) and by the Bulgarian National Science Fund under Contract No. 08-17 (B.O.).

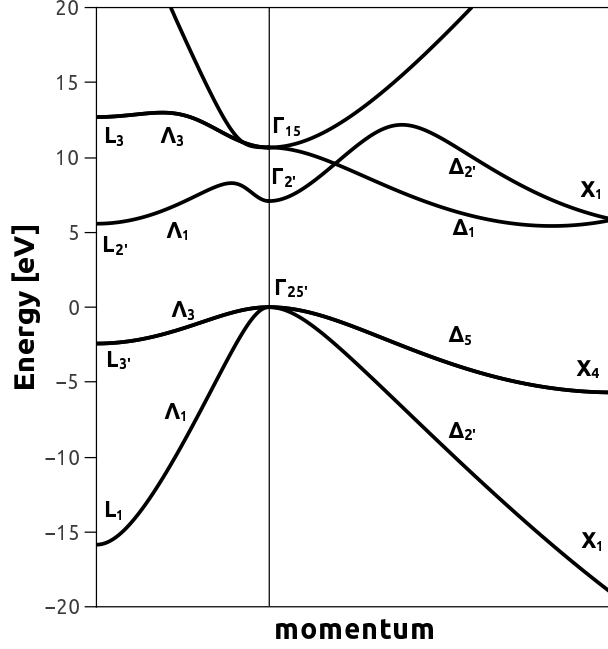


FIG. 1: Electronic energy bands of diamond along the Δ and Λ symmetry lines.

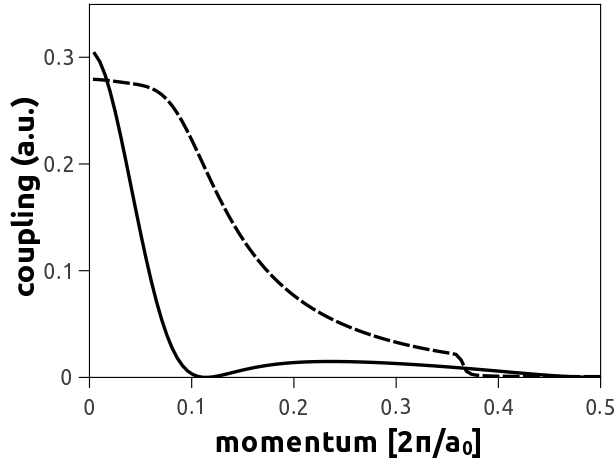


FIG. 2: Squared matrix elements of the component of the momentum onto the laser polarization direction between the light hole band and the lowest two conduction bands as a function of the crystal momentum $\mathbf{k} = k(1, 1, 1)$: $|\langle \Lambda_{1,th} | \mathbf{e} \cdot \mathbf{p} | \Lambda_{1,c} \rangle|^2$ (solid line) and $|\langle \Lambda_{1,th} | \mathbf{e} \cdot \mathbf{p} | \Lambda_{3,c} \rangle|^2$ (dashed line). The laser polarization vector \mathbf{e} is pointing along the $[111]$ direction.

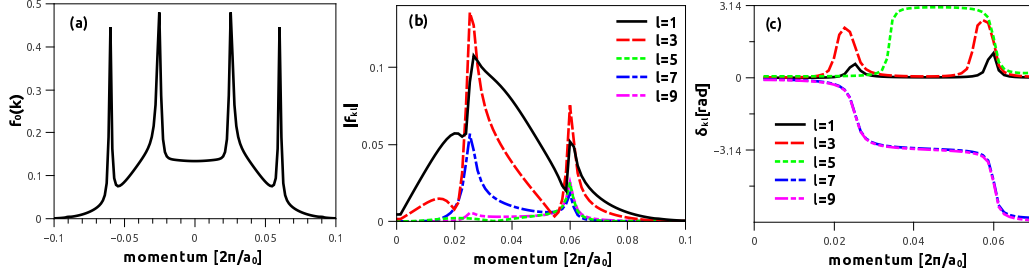


FIG. 3: (a) Cycle-averaged electron distribution function in bulk diamond along the Λ -line in the Brillouin zone. (b) Strength of laser-induced odd-order harmonics in diamond bulk along the same direction and Fig. (c) gives the corresponding phase shifts (in radians). In Figs. (a-c) the crystal is subjected to continuous wave laser with photon energy $\hbar\omega_L = 1.55$ eV, the electric field strength is $F = 0.4$ V/Å.

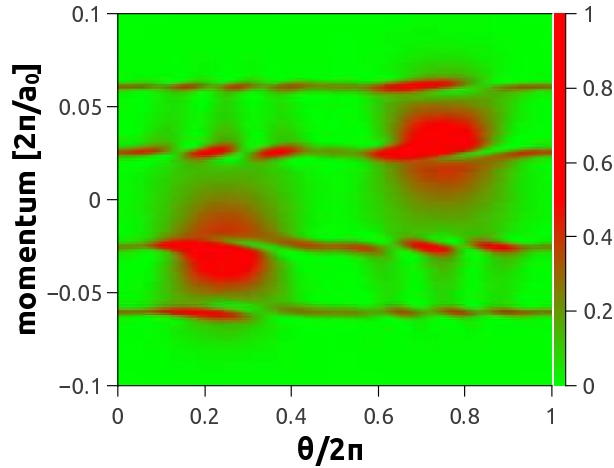


FIG. 4: (a) Temporal evolution of the electron distribution function in bulk diamond along the Λ line in the Brillouin zone for one period of oscillation of the electric field of a continuous wave laser having a photon energy $\hbar\omega_L = 1.55$ eV and field strength $F = 0.4$ V/Å, the phase parameter is $\theta = \omega_L t$.

¹ M. Drescher, M. Hentschel, R. Kienberger, G. Tempea, C. Spielmann, G. A. Reider, P. B. Corkum, and F. Krausz, *Science* **291**, 1923 (2001)

² T. J. Hammond, G. G. Brown, K. T. Kim, D. M. Villeneuve and P. B. Corkum, *Nat. Photon.*

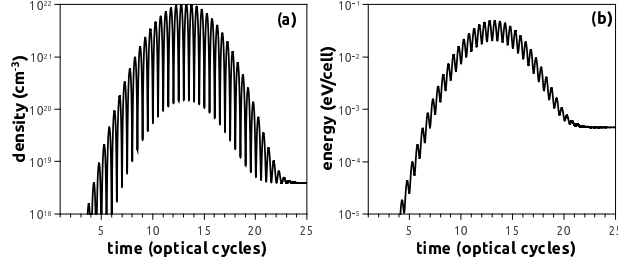


FIG. 5: (a) Time evolution of the electron density in diamond bulk irradiated by 15fs laser pulse with peak field strength $0.4 \text{ V}/\text{\AA}$, linearly polarized along the Λ line in the Brillouin zone and (b) Time development of the electronic excitation energy per unit cell. In Fig.(a-b) the time interval is measured in optical cycles of the laser field, one optical cycle has a duration of 2.75 fs

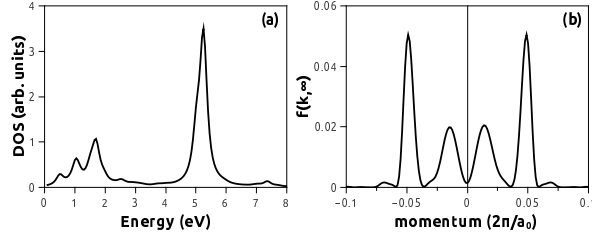


FIG. 6: (a) Density of conduction states after the irradiation of bulk diamond with 15fs laser pulse, having a peak intensity $0.4 \text{ V}/\text{\AA}$, linearly polarized along the Λ line in the Brillouin zone; energy is measured relative to the conduction band minimum. (b) Distribution function of electrons along the direction of laser polarization; the quasimomentum is measured in units $2\pi/a_0$, where $a_0 = 3.57 \text{ \AA}$ is the bulk lattice constant.

10, 171 (2016).

³ P. B. Corkum and F. Krausz, *Attosecond Science*, *Nat. Phys.*, **3**, 381 (2007).

⁴ F. Krausz and M. Ivanov, *Rev. Mod. Phys.* **81**, 163 (2009).

⁵ I. P. Christov, M. M. Murnane, and H. C. Kapteyn, *Optics Communications* **148**, 75 (1998)

⁶ K. B. Dinh, H. V. Le, P. Hannaford, L. V. Dao, *Optics Communications* **396**, 100 (2017)

⁷ O. Kfir, S. Zayko, C. Nolte, M. Sivilis, M. Möller, B. Hebler, S. S. Arekapudi, D. Steil, S. Schafer, M. Albrecht, O. Cohen, S. Mathias, C. Ropers, *Sci. Adv.*, **3**, eaao4641 (2017).

⁸ D. Rupp, N. Monserud, B. Langbehn, M. Sauppe, J. Zimmermann, Y. Ovcharenko, T. Möller, F. Frassetto, L. Poletto, A. Trabattini, F. Calegari, M. Nisoli, K. Sander, C. Peltz,

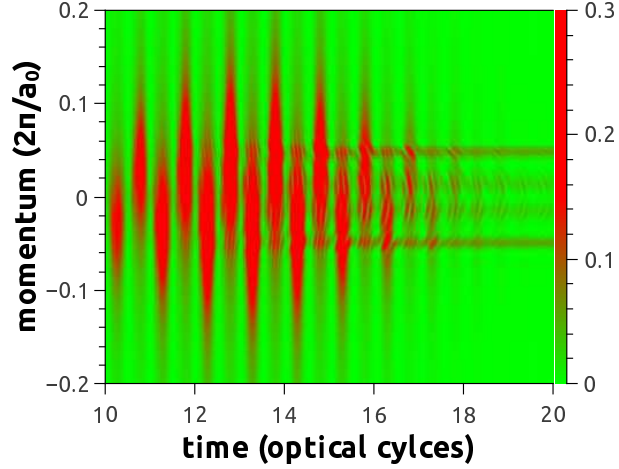


FIG. 7: Time evolution of the electron distribution function in bulk diamond along the Λ line in the Brillouin zone. The time interval is measured in optical cycles of the laser field, one optical cycle has a duration of 2.75 fs. The crystal momentum is measured in units $2\pi/a_0$, where $a_0 = 3.57 \text{ \AA}$ is the bulk lattice constant.

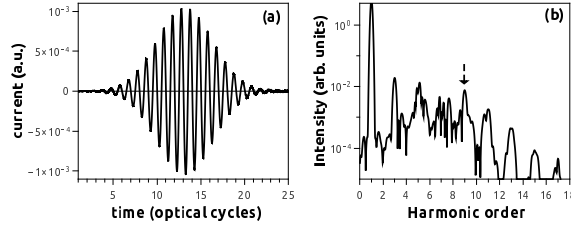


FIG. 8: (a) Time evolution of the optically-induced electronic current in bulk diamond irradiated by 15fs laser pulse of wavelength 800 nm, having peak field strength 0.4 V/\AA and linearly polarized along the Λ line in the Brillouin zone and (b) the corresponding spectrum of high-order harmonics.

M. J. Vrakking, T. Fennel and A. Rouzee, Nat. Comm. **8**, 493 (2017).

- ⁹ S. Ghimire, A. D. DiChiara, E. Sistrunk, P. Agostini, L. F. DiMauro and D. A. Reis, Nature Physics **7**, 138 (2011).
- ¹⁰ O. Schubert, M.Hohenleutner, F. Langer, B. Urbanek, C. Lange, U. Huttner, D. Golde, T. Meier, M. Kira, S. W. Koch, and R. Huber, Nat. Photonics **8**, 119 (2014).
- ¹¹ G. Ndabashimiye, S. Ghimire, M. Wu, D. A. Browne, K. J. Schafer, M. B. Gaarde and D. A. Reis, Nature **522**, 462 (2016).

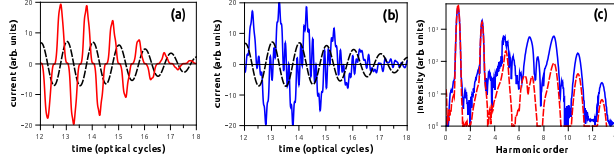


FIG. 9: (a) Time evolution of the optically-induced intraband current in the diamond bulk along the Λ line in the Brillouin zone and Fig. (b) gives the transient interband current along the same line. The dashed line in Fig.(a-b) indicates the temporal profile of the laser electric field and Fig.(c) includes the spectrum of the corresponding intraband (dashed line) and interband harmonics (solid line).

- ¹² T. T. Luu, M. Garg, S. Y. Kruchinin, A. Moulet, M. T. Hassan, and E. Goulielmakis, *Nature* (London) **521**, 498 (2015)
- ¹³ M. Schultze, K. Ramasesha, C. D. Pemmaraju, S. A. Sato, D. Whitmore, A. Gandman, J. S. Prell, L. J. Borja, D. Prendergast, K. Yabana, D. M. Neumark, S. R. Leone, *Science* **12**, 1348 1348 (2014).
- ¹⁴ A. Schiffrin, T. Paasch-Colberg, N. Karpowicz, V. Apalkov, D. Gerster, S. Muehlbrandt, M. Korbman, J. Reichert, M. Schultze, S. Holzner, J. V. Barth, R. Kienberger, R. Ernstorfer, V. S. Yakovlev, M. I. Stockman and F. Krausz, *Nature* **493**, 70 (2013).
- ¹⁵ G. Wachter, C. Lemell, J. Burgdrfer, S. A. Sato, X. Tong, and K. Yabana, *Phys. Rev. Lett.*, **113**, 087401 (2014).
- ¹⁶ T. Paasch-Colberg, S. Yu. Kruchinin, Özge Sağlam, S. Kapser, S. Cabrini, S. Muehlbrandt, J. Reichert, J. V. Barth, R. Ernstorfer, R. Kienberger, V. S. Yakovlev, N. Karpowicz, and A. Schiffrin, *Optica* **3**, 1358 (2016).
- ¹⁷ F. Krausz F and M. I. Stockman *Nat. Photonics* **8** 205, (2014).
- ¹⁸ G. Vampa, T. J. Hammond, N. Thiré, B. E. Schmidt, F. Légaré, C. R. McDonald, T. Brabec, P. B. Corkum, *Nature* **522**, 462 (2015)
- ¹⁹ T. Otobe, *Journal of Applied Physics* **111**, 093112 (2012), T. Otobe, K. Yabana, and J.-I. Iwata, *Journal of Computational and Theoretical Nanoscience* **6**, 2545 (2009).
- ²⁰ T. Otobe, *J. Appl. Phys.* **111**, 093112 (2012)
- ²¹ T. Otobe, *Phys. Rev. B* **94**, 235152 (2016)
- ²² I. Floss, C. Lemell, G. Wachter, V. Smejkal, S. A. Sato, X.-M. Tong, K. Yabana, and J.

- Burgdörfer, Phys. Rev. A **97**, 011401 (2017).
- ²³ N. Tancogne-Dejean, O. D. Mücke, F. X. Kartner and A. Rubio, Phys. Rev. Lett. **118**, 087403 (2017).
- ²⁴ T. Higuchi, M. I. Stockman, and P. Hommelhoff, Phys. Rev. Lett. **113**, 213901 (2014).
- ²⁵ M. Wu, S. Ghimire, D. A. Reis, K. J. Schafer, and M. B. Gaarde, Phys. Rev. A **91**, 043839 (2015).
- ²⁶ T. T. Luu and H. J. Weorner Phys. Rev. B **94**, 115164 (2016)
- ²⁷ G. Vampa, C. R. McDonald, G. Orlando, P. B. Corkum, and T. Brabec, Phys. Rev. B **91**, 064302 (2015)
- ²⁸ M. Lewenstein, Ph. Balcou, M. Yu. Ivanov, A. L’Huillier, and P. B. Corkum, Phys. Rev. A **49**, 2117 (1994).
- ²⁹ P. B. Corkum, Phys. Rev. Lett. **71**, 1994 (1993).
- ³⁰ T. Ikemachi, Y. Shinohara, T. Sato, J. Yumoto, M. Kuwata-Gonokami, and K. L. Ishikawa , Phys. Rev. A **95**, 043416 (2017)
- ³¹ K. K. Hansen, T. Deffge and D. Bauer, Phys. Rev. A **96**, 053418 (2017).
- ³² M. L. Cohen and T. K. Bergstresser, Phys. Rev. **141**, 789 (1966).
- ³³ A. D. Papadopoulos and E. Anastassakis, Phys. Rev. B **43**, 5090 (1991).
- ³⁴ L. A. Hemstreet Jr, C. Y. Fong, M. L. Cohen, Phys. Rev. B **2**, 2054 (1970).
- ³⁵ C. R. McDonald, G. Vampa, P. B. Corkum, and T. Brabec, Phys. Rev. A **92**, 033845 (2015).
- ³⁶ M. Cardona and F. H. Pollak, Phys. Rev. **142**, 530 (1966).